sustainability

MDPI

Article

Optimizing Solar Energy Harvesting through Integrated Organic Rankine Cycle–Reverse Osmosis Systems: A Techno–Economic Analysis

Lina Wang [1], Chunyu Zhou [2,*] and Hamid Reza Rahbari [3]

[1] School of Marine Technology and Environment, Dalian Ocean University, Dalian 116023, China; l.n.w@163.com
[2] Information Office, Dalian Ocean University, Dalian 116023, China
[3] AAU Energy, Aalborg University, 6700 Esbjerg, Denmark
* Correspondence: 15542572663@163.com; Tel.: +86-15542572663

Abstract: When it comes to seawater desalination in the small- to medium-electricity ranges, the organic Rankine cycle (ORC) powered by solar energy stands out as the most energy-efficient technology currently available. Various solar techniques have been developed to capture and absorb solar energy. Among them, the parabolic trough collector (PTC) has gained recognition as a low-cost solar thermal collector with a long operating life. This study investigates the thermodynamic performance and economic parameters of a PTC-powered ORC using Dowtherm A and toluene as working fluids for the solar cycle and ORC cycle, respectively. Thermo-economic multi-objective optimization and decision-making techniques are applied to assess the system's performance. Four key parameters are analyzed for their impact on exergy efficiency and total hourly cost. Using TOPSIS decision-making, the best solution from the Pareto frontier is identified, featuring an ORC exergy efficiency of 30.39% and a total hourly cost of 39.38 US$/h. The system parameters include a mass flow rate of fresh water at 137.7 m^3/h, a total output net power of 577.9 kJ/kg, and a district heating supply of 1074 kJ/kg. The cost analysis reveals that the solar collector represents approximately 68% of the total hourly cost at 26.77 US$/h, followed by the turbine, thermoelectric generator, and reverse osmosis (RO) unit.

Keywords: techno–economic optimization; exergy efficiency; ANN; NSGA-II; TOPSIS

check for updates

Citation: Wang, L.; Zhou, C.; Rahbari, H.R. Optimizing Solar Energy Harvesting through Integrated Organic Rankine Cycle–Reverse Osmosis Systems: A Techno–Economic Analysis. *Sustainability* **2023**, *15*, 13602. https://doi.org/10.3390/su151813602

Academic Editor: Luca Cioccolanti

Received: 13 July 2023
Revised: 27 August 2023
Accepted: 5 September 2023
Published: 12 September 2023

1. Introduction

The pressing global potable water crisis has swiftly risen to the forefront of our concerns, propelled by a confluence of factors, including rapid population expansion [1], burgeoning industrial progress [2], surging demands for freshwater resources [3], and the alarming depletion of our vital reserves [4]. According to the United Nations, more than 2.7 billion people are projected to face water scarcity challenges by the middle of this century. As civilization and industrialization advance, freshwater scarcity worsens, with predictions that two-thirds of the world's population will lack access to clean drinking water by 2025 [5]. In light of this situation, desalination—the process of converting seawater into potable water—has emerged as a viable solution, considering that over 97% of the Earth's water resources are seawater. However, the process of desalination demands a substantial amount of energy. To produce 22 million cubic meters of freshwater per day, approximately 203 million tons of oil are consumed annually [6]. Despite the unsustainability and significant environmental and public health risks associated with fossil fuels, they still contribute significantly to global energy consumption [7].

To address the challenge of greenhouse gas emissions, it is crucial to investigate alternative energy sources that can replace fossil fuels in the global energy supply [8]. Renewable energy options, such as solar, geothermal, and wind power, offer effective solutions for

reducing greenhouse gas emissions. The European Union (EU) has set ambitious targets for its economy, aiming to achieve "zero-emissions" by 2050 and work towards energy independence, as outlined in the European Green Deal policy introduced in 2019 [9].

Solar energy, with its advantages of being a free and limitless source while reducing the consumption of non-renewable primary energy, is an excellent option for achieving zero emissions [10]. Solar energy can be broadly categorized into two main types: solar photovoltaic (PV) technology, which directly converts solar energy into electricity, and solar thermal collectors, which concentrate solar energy to generate heat [11]. Within the realm of solar thermal collector diversity, parabolic trough collectors (PTC) stand out as a widely adopted choice, especially well-suited for scenarios necessitating a moderate level of temperature concentration (up to 500 °C) [12]. Their inherent cost-effectiveness and remarkable efficiency make them a compelling option for such applications [13]. PTCs can be easily integrated with traditional power plants, such as steam turbines (Rankine cycle) or gas turbines (Brayton cycle), to enhance overall system efficiency while minimizing environmental impact [14].

An effective technique for converting heat into power is the organic Rankine cycle (ORC) below 400 °C [15]. The ORC operates on the same principles as the conventional Rankine cycle but utilizes organic fluids with lower saturation temperatures as the working fluid (WF) instead of water [16]. Considering sustainable development as a paramount factor, the potential WF for ORC systems encompass a range of options, including natural refrigerant choices such as carbon dioxide and hydrocarbons. Alongside these, there are hydrofluorocarbons and various combinations of WFs that also warrant consideration [17]. The ORC system consists of four essential components: the evaporator, turbine, pump, and condenser [18]. The efficiency of the ORC system is profoundly impacted by both the operational parameters and system coupling factors. These include crucial elements such as integration crucial temperature and pressure [19].

Reverse osmosis (RO) and thermal procedures, such as multi-stage flash (MSF) and multi-effect distillation (MED), are the two main classes of membrane technology that have been proposed as water desalination techniques [20]. The commercialization of MSF and MED technologies is constrained by their substantial energy requirements, encompassing two key components: thermal energy for the evaporation process and electricity to power pumps and other plant operations [21]. For each cubic meter (m^3) of produced water, MSF desalination facilities operating at temperatures exceeding 110 °C require approximately 3.5 kWh of electricity and around 12 kWh of thermal energy. In contrast, MED plants operating at temperatures below 70 °C exhibit reduced power requirements, with about 1.5 kWh of electrical energy and 6 kWh of thermal energy [22].

Compared to other techniques, RO currently dominates the industry due to several reasons. Firstly, RO can accommodate a wide range of production capacities, ranging from small standalone installations to large-scale operations capable of producing up to 500,000 m^3 per day. Secondly, RO plants can operate continuously and reliably for extended periods without the need for shutdowns. Lastly, RO exhibits low specific energy consumption, typically ranging from 2 to 4 kWh/m^3, which approaches the thermodynamic limit of 1 kWh/m^3 for seawater desalination. In terms of environmental impact, the CO_2 emissions of RO range from 1.7 to 2.8 kg/m^3, making it the most environmentally friendly option compared to other techniques [23]. Hence, the optimal approach for seawater desalination is employing the RO technique.

The commercialization of parabolic trough collector (PTC) based systems encounters notable constraints, primarily centered around the aspects of elevated total costs and intermittent operation. Addressing the intermittency concern, the integration of storage tanks has been introduced as a strategic measure within the system. In addition, to evaluate the performance of the system, a more advanced model is created based on machine learning. The main focus of this work is to design an advanced heat and power multi-generation ORC system. To significantly enhance energy efficiency, the integration of the heat exchanger (HE) and thermoelectric generator (TEG) into the system has been successfully achieved.

Additionally, the power generated by this setup is effectively utilized by the RO system to produce clean water. The ORC system modeling has been accomplished by leveraging the working fluid properties and considering the thermodynamic constraints using the Engineering Equation Solver (EES). Artificial Neural Network (ANN) technology functions akin to the human brain. In contrast to thermodynamic modeling, the utilization of ANN can significantly reduce optimization time. By employing ANN, intricate optimization challenges can be simplified, streamlining the process and concurrently enhancing the ANN's structural parameters. After modeling, the stochastic data generated by EES is inputted into the ANN, further streamlining the optimization process. This approach significantly contributes to the innovation of this article, and the following factors highlight its uniqueness and novelty:

- The integration of EES with ANN has demonstrated a remarkable reduction in optimization time. Additionally, the incorporation of HE and TEG measures has led to substantial enhancements in the exergy efficiency of the system. These advancements collectively underscore the significance of coupling advanced methodologies for optimizing energy systems and underline the potential for achieving superior performance and efficiency. The thermodynamic processes involved in the ORC system, such as compression, expansion, evaporation, and regeneration, are modeled using an ANN. This advanced modeling technique utilizes the properties of the WF to accurately predict and evaluate the system's performance during each process. This approach significantly enhances the accuracy and reliability of performance predictions in the ORC system.
- The utilization of NSGA-II, a powerful multi-objective optimization technique, allows for the achievement of optimal design and operating setpoints in the ORC system. This integration is pivotal in enhancing the system's economic viability while optimizing its exergy efficiency.
- The Technique for Order Preference by Similarity to Ideal Situation (TOPSIS) method is employed as the decision-making tool to determine the best solution for the multi-generation system. This approach aids in selecting the most optimal configuration by considering various criteria and evaluating the system's performance against ideal solutions.
- The optimization process focuses on increasing the exergy efficiency, reducing the production cost of desalinated water, and enhancing the co-generation capabilities.

2. Literature Review

The principal objective of the proposed system is twofold: to curtail the overall costs and enhance operational efficiency. Within the realm of efficiency augmentation, the integration of HE and TEG emerges as a particularly potent strategy. These measures represent a compelling avenue for elevating system performance, exemplifying a paramount approach among the spectrum of available enhancement techniques. Jafary et al. proposed a trigeneration system based on PTC and organic Rankine cycle (ORC) and investigated the impact of an internal heat exchanger in detail. The results demonstrated that the inclusion of an internal heat exchanger increased the exergy efficiency of the system from 6.641% to 12.69% [24]. Aliahmadi et al. conducted a comparative analysis involving three distinct plants, revealing a compelling correlation between the highest plant efficiency and the greatest power output derived from the TEG unit [25].

An additional efficacious approach for enhancing system efficiency involves the selection of the optimal WF. Yu et al. introduced a design system that combines solar energy with the ORC. Four different WFs were thoroughly investigated, and under optimal conditions toluene exhibited the best performance among them, resulting in a system exergy efficiency of 24.8% [26]. Li et al. also presented an ORC driven by waste heat recovery, exploring cyclohexane, benzene, and toluene as the WFs. According to their findings, toluene outperformed the other high-temperature WFs [27]. A PTC-based hybrid system was proposed by Razmi et al. [28]. To select the optimal working fluid and ideal operating

conditions for solar installations, five WFs were compared in detail. The results showed that DowthermA was the best choice.

For achieving optimal cost reduction, cogeneration stands out as the most efficient approach. Rostami et al. explored a PTC-based electricity storage system for trigeneration, which produced 22.5 kW of power, 140.8 kW of heat, and 97.3 g/h of hydrogen [29]. Furthermore, Alotaibi et al. conducted a comparison between a PTC-based power plant and an equivalent photovoltaic solar plant. The study revealed that the PTC solar plant had a 45% lower ideal aperture area and a 44% lower Levelized Cost of Energy (LCOE) compared to the photovoltaic solar plant [30].

Richard's team has made significant strides in the field of renewable energy-powered membrane technology. Their efforts have been particularly directed towards studying the impact of fluctuating solar irradiance. The system can function effectively with a variable energy source, especially if extra power is made available to kick-start it after a period of shutdown [31]. Boussouga et al. conducted a thorough investigation into the properties of RO membranes [32]; in terms of permeate quality, tight nanofiltration/RO membranes display a strong resilience. Li et al. [33] additionally highlight that, by employing a motor power rating of less than 1.5 kW, it is conceivable to achieve a specific energy consumption ranging from 1.5 to 3 kWh/m^3, as estimated. The average specific energy consumption has also experienced a significant decrease. For instance, in 2005, Schäfer and Richard conducted a case study in an Australian remote national park, where the specific energy consumption was measured at 5 kWh/m^3 [34]. In 2016, Shen et al. presented a case study in Tanzania, in which the specific energy consumption was 1.6 kWh/m^3 [35].

In a study by Amin et al., an analysis of three cascade power plants connected to an RO desalination unit driven by a solar pond was presented. The study concluded that, for the proposed system, June is the most cost-effective month with a product cost of \$72.42/kWh [36]. Dong et al. introduced a pioneering hybrid solar–geothermal system with an RO subsystem. The system exhibited remarkable exergy efficiency, achieving an impressive 3%. Additionally, the unit exergy cost was determined to be \$19.77/GJ, showcasing its economic viability [37].

In the field of ORC, machine learning techniques have garnered increasing attention due to their self-learning capabilities, ability to handle nonlinearity, and capacity to approximate arbitrary functions. ANN technology, renowned for these attributes, has been frequently utilized in developing prediction models [38]. Zhou and colleagues undertook an extensive study comparing optimization times between ANN and mechanistic models. The findings reveal that ANN achieves an optimization time of approximately 0.135 s, whereas mechanistic models require over 10 h. Notably, the accuracy rate of ANN impressively reaches 99% [39]. By leveraging an ANN-based model, remarkable levels of optimization and design detail were attained by Chen et al., the results demonstrating that the model reduces calculation time by more than 50% [40]. The primary purpose of ANN is to expedite calculations, and it is frequently employed in conjunction with optimization algorithms to enhance their performance.

The Non-Dominated Sorting Genetic Algorithm (NSGA-II) is an influential decision space exploration engine that is based on the Genetic Algorithm (GA) framework. It is specifically designed for effectively solving Multi-objective Optimization Problems (MOOPs) [41]. NSGA-II was originally proposed by Deb et al. [42] and has since proven to be a powerful and widely utilized approach in the field. The NSGA-II algorithm was utilized to conduct a multi-objective thermo–economic optimization of biomass retrofit for an existing solar ORC power plant to identify the most efficient and cost-effective solutions [43]. Xu et al. employed NSGA-II to explore the optimal configuration of a standalone wind/PV/hydrogen system to identify a set of Pareto solutions [44]. The Pareto front provides a series of equivalent solutions for the multi-objective problem, each offering a balanced trade-off between the objectives being considered. In this work, the final Pareto frontier solution is selected through the utilization of the TOPSIS approach, which was originally developed by Hwang and Yoon in 1981 [45]. It is a statistical technique that aims

to optimize the selection process by increasing the gap from a negative ideal solution and decreasing the gap from a positive ideal solution, ultimately identifying the most favorable choice among a given set of alternatives. Additionally, the proximity to the positive ideal solution serves as a significant criterion for evaluating the top-ranked option [46].

Based on the aforementioned literature survey, it becomes evident that the co-generation of heat and power offers a potent avenue for substantially diminishing the overall investment costs within the system. Furthermore, the integration of a seawater desalination component remarkably enhances the economic viability of the entire setup. The proposition entails a co-generation system founded on PTC technology, harmoniously integrated with an RO subsystem. For the PTC cycle, DowthermA was judiciously selected as the WF, while toluene assumed its role within the ORC cycle. Thermodynamic modeling was conducted using EES to showcase the optimal performance of the proposed system. To further enhance this performance, a dual optimization approach employing ANN and NSGA-II was employed. Additionally, the TOPSIS decision-making method was applied to identify the most favorable solution.

3. Materials and Methods

The schematic diagram depicting the integration of the solar collector cycle, the ORC system, and the RO unit is shown in Figure 1. This coupling arrangement showcases the interconnectedness and interplay of these components within the overall system. The WF of the solar cycle is Dowtherm A. The WF is heated by a solar collector during the daytime when there is sunshine. It then flows into the hot tank (HT). After undergoing heat exchange with the evaporator and economizer, the WF, now at a lower temperature, returns to the cold tank (CT), where it awaits reheating once again by the solar collector. In the ORC, the WF used is toluene. The WF is preheated at point 8 by the economizer, and subsequently undergoes heat exchange in the evaporator. As a result of this heat exchange process, the WF transforms into vapor, which is observed at point 10. The vapor expands through the turbine to generate power. A portion of the vapor is extracted and directed towards the open feed organic fluid heater (OFOH), while the remaining WF flows towards the HE. At point 14, the WF undergoes heat exchange before proceeding to the TEG to further enhance system efficiency and generate power. Subsequently, the two portions of the WF are mixed again at the OFOH and, after passing through pump 3, return to the economizer to complete the cycle. The power generated by the turbine and TEG are utilized in the RO system for the production of desalinated water.

A comprehensive analysis of the proposed system is imperative to assess its performance thoroughly. This analysis should encompass energy, exergy, and economic aspects, taking into account the baseline values and design conditions specified in Table 1.

Table 1. Design parameters and input values for the suggested system's parts.

Subsystem	Parameters	Symbol	Value	Unit
PTC [28]	Absorptivity of receiver	α	0.96	-
	heat loss coefficient	U_L	3.82	$W/m^2 \cdot °C$
	Correction factor for diffuse radiation	γ	0.95	-
	Effective transmissivity	τ_p	0.94	-
	Heat transfer coefficient inside the receiver	h_{fi}	300	$W/m^2 \cdot °C$
	Receiver inside diameter	$D_{i,r}$	0.066	m
	Receiver outside diameter	$D_{o,r}$	0.07	m
	Single collector length	L	12.27	m
	Single collector width	W	5.76	m
	Thermal conductivity of the receiver	K	16	$W/m^2 \cdot °C$
	Transmissivity of the cover glazing	τ_c	0.96	-
	Direct normal irradiance	G_b	850	W/m^2

Table 1. *Cont.*

Subsystem	Parameters	Symbol	Value	Unit
RO [47]	membrane permeability resistance	K_m	8.03×10^{-11}	$m^2 \cdot s/(kg \cdot Pa)$
	total number of membranes	n	600	-
	the number of trains	b_n	7	-
	Number of pressure vessels	N_P	42	-
	Recovery ratio	RR	0.3	-
	Seawater salinity	X_{20}	45	g/kg

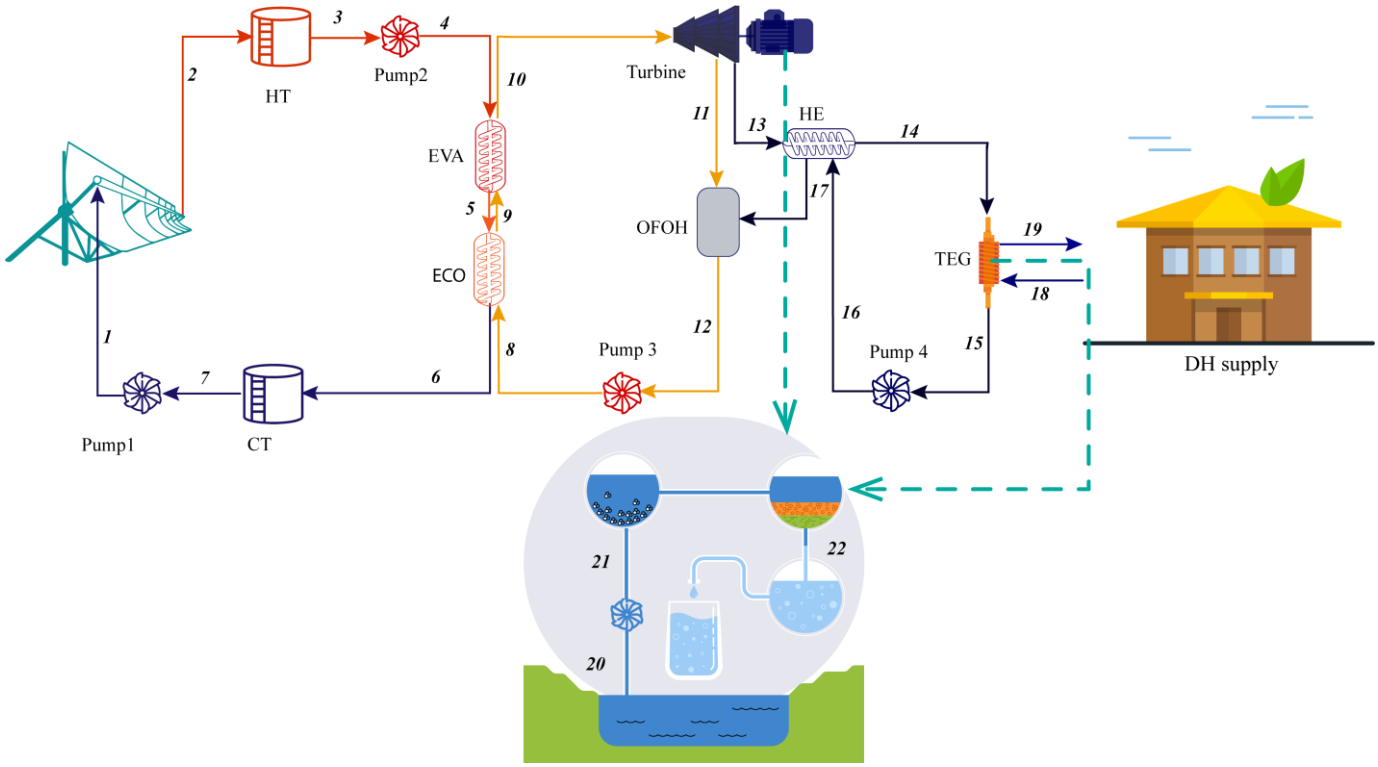

Figure 1. Schematic of combined PTC and ORC with RO plant.

3.1. Energy Analysis

The following are the presumptions taken into account when simulating the system configurations:

- For modeling all the components, a steady-state condition is taken into consideration;
- Kinetic and potential energy changes are disregarded;
- 298.15 K and 101.3 kPa are the ambient temperature and pressure, respectively;
- Pump and turbine isentropic efficiency are 80% and 85%, respectively.

3.1.1. Parabolic Trough Collector (PTC)

During the daytime, the solar collector absorbs the heat from the sun, and the heat transfer rate is [48]:

$$\dot{Q}_u = N \cdot F_R \cdot [(S_{AR} \cdot A_a) - (A_r \cdot U_L \cdot (T_{in} - T_0))] \quad (1)$$

$$\dot{Q}_u = \dot{m}_2 (h_2 - h_1) \quad (2)$$

where N is the number of collectors, and A_a and A_r represent the areas of the aperture and receiver, respectively. Additionally, U_L denotes the heat loss coefficient of the collector, while T_{in} and T_0 refer to the inlet temperature of the collector and room temperature,

respectively. F_R represents the heat loss factor, The absorbed solar radiation, denoted as $S_{AR,}$ can be calculated as follows [49]:

$$S_{AR} = G_b \cdot \tau_c \cdot \tau_p \cdot \gamma \cdot \alpha \tag{3}$$

While the heat loss factor is:

$$F_R = \frac{\dot{m}_{CL} \cdot C_{p,CL}}{A_r \cdot U_L} \cdot \left(1 - exp\left(-\frac{A_r \cdot U_L \cdot F_{CL}}{\dot{m}_{CL} \cdot C_{p,CL}}\right)\right) \tag{4}$$

where the $\dot{m}_{CL}$ represents the mass flow rate of the WF, and F_{CL} denotes the efficiency factor of the PTC, which is determined by the following calculation:

$$F_{CL} = \frac{U_L^{-1}}{U_L^{-1} + \frac{D_{o,r}}{h_{fi}} + \left(\frac{D_{o,r}}{2k} \cdot ln \frac{D_{o,r}}{D_{i,r}}\right)} \tag{5}$$

where k represents the thermal conductivity of the receiver, D denotes the diameter, and the subscripts i and o represents the inside and outside, respectively. The area of the aperture can be determined as follows:

$$A_a = L_{CL} \cdot (W - D_{o,r}) \tag{6}$$

where L_{CL} and W are the length and width of the receiver.

3.1.2. Thermoelectric Generator (TEG)

Through the implementation of the Seebeck effect, TEGs have demonstrated their ability to directly convert thermal energy into electric power. A TEG consists of three essential components: a heat exchanger, thermoelectric modules, and a heat sink. The functioning of a TEG is governed by the temperature disparity between the two sides of the generator [50]. In order to achieve optimal efficiency in thermoelectric energy conversion, the thermoelectric figure of merit (ZT_M) is typically employed. Enhancements in the ZT_M value led to a corresponding increase in thermoelectric efficiency. ZT_M can be calculated as [51]:

$$ZT_m = \frac{\psi^2 T_m}{KR} \tag{7}$$

where K denotes the thermal conductivity, T_m is the mean temperature, and R is the resistance within the TEG, ψ is the Seebeck coefficient, which is defined as:

$$\psi = -\frac{\Delta V}{\Delta T} \tag{8}$$

$$T_m = \frac{1}{2}(T_H + T_L) \tag{9}$$

$$T_H = \frac{1}{2}(T_{14} + T_{15}) \tag{10}$$

$$T_L = \frac{1}{2}(T_{18} + T_{19}) \tag{11}$$

Here, T and V denote the temperature and voltage, respectively. The subscript H and L represent the high temperature and low temperature of the TEGs. The efficiency of the TEG is:

$$\eta_{TEG} = \eta_C \frac{\sqrt{1 + ZT_m} - 1}{\sqrt{1 + ZT_m} + \frac{T_L}{T_H}} \tag{12}$$

$$\eta_C = 1 - \frac{T_L}{T_H} \tag{13}$$

where η_C is the Carnot efficiency, and the energy balance of the TEG unit can be shown as [52]:

$$\dot{m}_{14}h_{14} + \dot{m}_{18}h_{18} = \dot{m}_{15}h_{15} - \dot{m}_{19}h_{19} + \dot{W}_{TEG} \tag{14}$$

$$\eta_{TEG} = \frac{\dot{W}_{TEG}}{\dot{m}_{14}(h_{14} - h_{15})} \tag{15}$$

3.1.3. Reverse Osmosis (RO)

The mass conservation equation for each component, along with the recovery ratio, is utilized to determine the water mass flow rate in each pipe and its corresponding salinity. The recovery ratio is defined as the proportion of feed water to fresh water [53]:

$$RR = \frac{\dot{m}_{FW}}{\dot{m}_{feedwater}} = \frac{\dot{m}_{22}}{\dot{m}_{20}} \tag{16}$$

The energy balance equation can be described as [54]:

$$\dot{W}_{RO} = b_n(\dot{W}_{HPP} - \dot{W}_{HPT}) \tag{17}$$

$$\dot{W}_{HPP} = \frac{\Delta P \dot{m}_{20}}{\rho_{20}\eta_{HPP}} \tag{18}$$

$$\dot{W}_{HPT} = \frac{\Delta P \dot{m}_{22}\eta_{HPT}}{\rho_{22}} \tag{19}$$

where $\dot{W}_{HPP}$ and $\dot{W}_{HPT}$ represent the power of the pump and turbine in the RO unit, b_n refers to the number of trains, and $\dot{W}_{RO}$ denotes the net power required by the RO plant. ΔP refers to the transmembrane pressure, η_{HPT} and η_{HPP} denote the isentropic efficiencies of the turbine and pump respectively, and ρ represents the density.

$$\Delta P = \Delta\pi + J_w \mathrm{K}_m \tag{20}$$

$$J_w = \frac{\dot{m}_{22}}{\rho_{22} n A_{mem}} \tag{21}$$

$$\Delta\pi = 8.051 \times 10^7 C_w R \tag{22}$$

where J_w denotes volumetric permeate flow rate, K_m represents the membrane permeability resistance, $\Delta\pi$ denotes the transmembrane osmotic pressure, n is the number of membranes, A_{mem} is the area of membranes, and C_w is the membrane wall concentration, which can be described as:

$$C_w = \frac{e^{\left(\frac{Jw}{K_{mass}}\right)} x_{20}}{e^{\left(\frac{Jw}{K_{mass}}\right)}(1 - R_C) + R_C} \tag{23}$$

$$K_{mass} = 0.04 Re^{0.75} Sc^{0.33} \frac{D_s}{d} \tag{24}$$

Here, K_{mass} is the mass transfer coefficient and R_C is the membrane rejection. Furthermore, Sc and Re denote the Schmidt and Reynolds numbers, respectively. The Schmidt and Reynolds numbers can be calculated as follows:

$$Re = \frac{\dot{m}_{20}}{N_{ch} L_W N_P \mu_{20}} \tag{25}$$

$$Sc = \frac{\mu_{20}}{\rho_{20} D_s} \tag{26}$$

where N_P and N_{ch} represent pressure vessels and feed channel numbers, respectively.

3.1.4. Organic Rankine Cycle (ORC)

The WF of this cycle is toluene, and the heat transfer from the economizer can be described as:

$$\dot{m}_8(h_9 - h_8) = \dot{m}_5(h_5 - h_6) \tag{27}$$

$$\dot{Q}_{Eco} = \dot{m}_8(h_9 - h_8) \tag{28}$$

where $\dot{m}$ denotes the mass flow rate of the WF, and h represents the enthalpy of each state. The equation presented below is utilized to ascertain the precise amount of heat that the evaporator provides to initiate its cycle [55]:

$$\dot{m}_9(h_{10} - h_9) = \dot{m}_5(h_4 - h_5) \tag{29}$$

$$\dot{Q}_{Eva} = \dot{m}_9(h_{10} - h_9) \tag{30}$$

The following represents the output power generated by the turbine:

$$\dot{W}_{Tur} = \dot{m}_{10} h_{10} - \dot{m}_{11} h_{11} - \dot{m}_{13} h_{13} \tag{31}$$

$$h_{11} = h_{10} - \eta_{Tur}(h_{10} - h_{11s}) \tag{32}$$

where η_{Tur} is the isentropic efficiency of the turbine. The heat transfer of HE also can be described as:

$$\dot{Q}_{IHE} = \dot{m}_{13}(h_{13} - h_{14}) = \dot{m}_{16}(h_{17} - h_{16}) \tag{33}$$

The energy balance based on the first law for OFOH is:

$$\dot{m}_{12} h_{12} = \dot{m}_{11} h_{11} + \dot{m}_{17} h_{17} \tag{34}$$

The useful work and pump operation of the ORC are derived based on the following equations:

$$\dot{W}_{Net} = \dot{W}_{Tur} + \dot{W}_{TEG} - \dot{W}_{Pump3} - \dot{W}_{Pump4} \tag{35}$$

$$\dot{W}_{Pump3} = \dot{m}_{12}(h_8 - h_{12}) \tag{36}$$

$$\dot{W}_{Pump4} = \dot{m}_{15}(h_{16} - h_{15}) \tag{37}$$

3.2. Exergy Balance

Exergy serves as a reflection of the thermodynamic characteristics of a system, encompassing potential exergy, chemical exergy, physical exergy, and kinetic exergy as its primary components. This present work only considers physical exergy aspects within the system. The following equation is employed for quantifying the exergy content within each unit:

$$\dot{E}_{xi} = \dot{m}[(h_i - h_0) - T_0(s_i - s_0)] \tag{38}$$

where h_0 and s_0 represent the enthalpy and entropy of the WF at standard ambient pressure and room temperature. Based on the second law of thermodynamics, the exergy balance equation for each unit is expressed in the following form:

$$\dot{E}_{x_Q} + \sum \dot{E}_{xi} = \sum \dot{E}_{xe} + \dot{E}_{x_w} + \dot{E}_{x_D} \tag{39}$$

$$\dot{E}_{x_Q} = \left(1 - \frac{T_0}{T}\right) Q \tag{40}$$

$$\dot{E}_{x_w} = W \tag{41}$$

$\dot{E}_{x_Q}$ denotes the exergy resulting from heat transfer, while $\dot{E}_{x_w}$ signifies the exergy resulting from work, and $\dot{E}_{x_D}$ represents the exergy destruction. The exergy efficiency of the ORC is defined as:

$$\eta_{EX} = \frac{\left(\dot{W}_{Net} + \dot{E}_{x19}\right) \cdot t_{Day}}{\dot{E}_{x_{Sun}} \cdot t_{Sun} + \dot{E}_{x18} \cdot t_{Day}} \tag{42}$$

where t_{Sun} and t_{Day} denote the time of sun radiation (10 h) and one day (24 h). The exergy balance equations for each component are presented in Table 2.

Table 2. The exergy balance equations of each component.

Component	Exergy Balance Equations
Solar collector	$\dot{E}_{x_{Sun}} + \dot{E}_{x1} = \dot{E}_{x2} + \dot{E}_{x_{DSun}}$
HT	$\dot{E}_{x2} = \dot{E}_{x3} + \dot{E}_{x_{DHT}}$
CT	$\dot{E}_{x6} = \dot{E}_{x7} + \dot{E}_{x_{DCT}}$
Pump1	$\dot{E}_{x7} + \dot{W}_{Pump1} = \dot{E}_{x1} + \dot{E}_{x_{DPump1}}$
Pump2	$\dot{E}_{x3} + \dot{W}_{Pump2} = \dot{E}_{x4} + \dot{E}_{x_{DPump2}}$
Evaporator	$\dot{E}_{x9} + \dot{E}_{x4} = \dot{E}_{x5} + \dot{E}_{x10} + \dot{E}_{x_{DEva}}$
Economizer	$\dot{E}_{x5} + \dot{E}_{x8} = \dot{E}_{x6} + \dot{E}_{x9} + \dot{E}_{x_{DEco}}$
Turbine	$\dot{E}_{x10} = \dot{E}_{x11} + \dot{E}_{x13} + \dot{W}_{Tur} + \dot{E}_{x_{DTur}}$
Pump3	$\dot{E}_{x12} + \dot{W}_{Pump3} = \dot{E}_{x8} + \dot{E}_{x_{DPump3}}$
OFOH	$\dot{E}_{x11} + \dot{E}_{x17} = \dot{E}_{x12} + \dot{E}_{x_{DOFOH}}$
HE	$\dot{E}_{x13} + \dot{E}_{x16} = \dot{E}_{x14} + \dot{E}_{x17} + \dot{E}_{x_{DIHE}}$
TEG	$\dot{E}_{x14} + \dot{E}_{x18} = \dot{E}_{x15} + \dot{E}_{x19} + \dot{E}_{x_{DTEG}}$
Pump4	$\dot{E}_{x15} + \dot{W}_{Pump4} = \dot{E}_{x16} + \dot{E}_{x_{DPump4}}$

3.3. Economic Analysis

A thorough understanding of energy systems can be obtained by taking into account economic analyses, particularly hourly costs. The rates for plant investment costs, maintenance costs, labor wages, plant overhead and administration costs, insurance costs, local taxes, and royalty costs are added up to create the rate for plant development and operation. The following formula could be used to calculate the investment cost rate [56]:

$$\dot{Z}_{tot} = \frac{Z \cdot CRF \cdot \varphi}{\tau} \tag{43}$$

where Z stands for the capital invested in the plant, CRF for the capital recovery factor (0.11), φ for the maintenance factor (1.06), and τ for the number of working hours per year (7446 h). The CRF is defined as:

$$CRF = \frac{i \cdot (1+i)^n}{(1+i)^n - 1} \tag{44}$$

where i is the interest rate (0.1) and n denotes the reactor duration (20 years). The pivotal determinant influencing overall investment assessment lies within the heat transfer area, a critical component particularly impactful in heat exchanger costing. One illustrative depiction of the heat exchanger is as follows [57]:

$$Q_i = \Delta T_m A_i U_i \tag{45}$$

where Q_i is the flow rate of heat transfer, A_i denotes the heat transfer area, and U_i signifies the coefficient of heat transfer. In addition, the Logarithmic Mean Temperature Difference (LMTD), which may be mathematically defined as ΔT_m, is represented by [58]:

$$\Delta T_m = \frac{\Delta T_1 - \Delta T_2}{ln\frac{\Delta T_1}{\Delta T_2}} \tag{46}$$

Table 3 provides the economic information that was used in the calculations.

Table 3. The investment cost rate of each component [47].

Component	Capital Expense Function (US$)
Solar collector	$Z_{SC} = 240A_aN$
Evaporator	$Z_{Eva} = 276A_{Eva}^{0.88}$
Economizer	$Z_{Eco} = 276A_{Eco}^{0.88}$
Pumps	$Z_{Pump} = 3540\dot{W}_{Pump}^{0.71}$
TEG	$Z_{TEG} = 1500\dot{W}_{TEG}$
Turbine	$Z_{Tur} = 4750\dot{W}_{Tur}^{0.7}$
HE	$Z_{IHE} = 12000\left(\frac{A_{IHE}}{100}\right)^{0.6}$
OFOH	$Z_{OFOH} = 145.315(\dot{Q}_{OFOH})^{0.6}$
RO desalination	$Z_{RO} = 0.98(\dot{m}_{FW})^{0.67}$

4. Results and Discussion

The thermodynamic properties of the system are analyzed using EES. The working fluid for the solar cycle is DowthermA, known for its excellent heat transfer properties. To expedite the calculation process, an ANN is incorporated into the simulation. ANN is a well-established machine-learning algorithm, renowned for its simplicity, ease of implementation, and exceptional performance across various applications [59]. Notably, a three-layer backpropagation neural network can approximate a rational function with remarkable precision. In this study, a three-layer BP network is employed to describe the thermodynamic processes based on the working fluid parameters. These layers include the input layer, hidden layer, and output layer.

Figure 2 illustrates the comprehensive system flowchart. The procedural sequence unfolds as follows: initial data generated during EES modeling were seamlessly channeled into the ANN framework to streamline the modeling procedure. Subsequently, the optimization phase was orchestrated through NSGA-II to yield a Pareto frontier. Finally, the judicious application of the TOPSIS decision-making approach culminated in the selection of the most optimal solution for the system.

Upon concluding the entire modeling process, EES generated a dataset comprising 1000 random data points. These data points were derived from the optimization parameter range. Table 4 presents the optimal parameters along with their respective ranges of variation. In consideration of both the economic property and system performance, the total hourly investment ($\dot{Z}_{tot}$) and the exergy efficiency of the ORC (η_{EX}) were chosen as the output optimization variables. To construct accurate ANN models for thermodynamic processes, a substantial amount of data is necessary for network training. Thus, this study utilized the 1000 random data points obtained from EES.

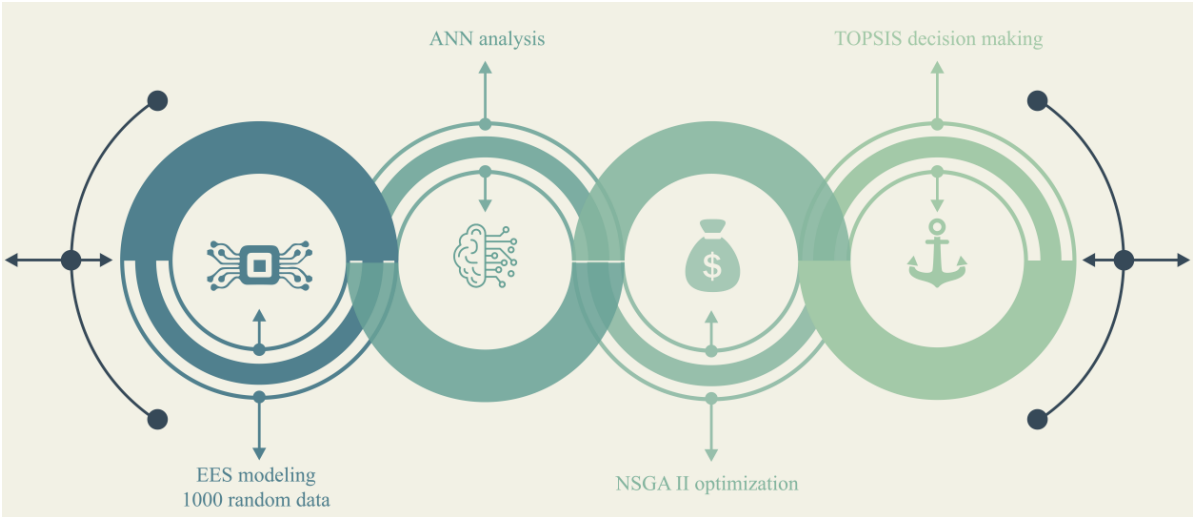

Figure 2. The flowchart of the proposed system.

Table 4. The logical range of the operating parameters.

Parameters	Upper Bond	Lower Bond
T_{15} (°C)	90	70
T_2 (°C)	400	370
T_{10} (°C)	280	240
A_{Tol} (m^2)	10,000	7000

The 1000 random data points were divided into three distinct parts for training, testing, and validation purposes. Specifically, 70% of the data was allocated for training, while 15% was set aside for testing. The remaining 15% was utilized for validation. The model's validation results are illustrated in Figure 3. The accuracy of the ANN is evaluated using the coefficient of determination (R). A higher value of R indicates a greater accuracy of the neural network's predictions. As the value approaches unity, the forecast of the neural network becomes increasingly precise. This observation is depicted in Figure 3, confirming the model's exceptional accuracy.

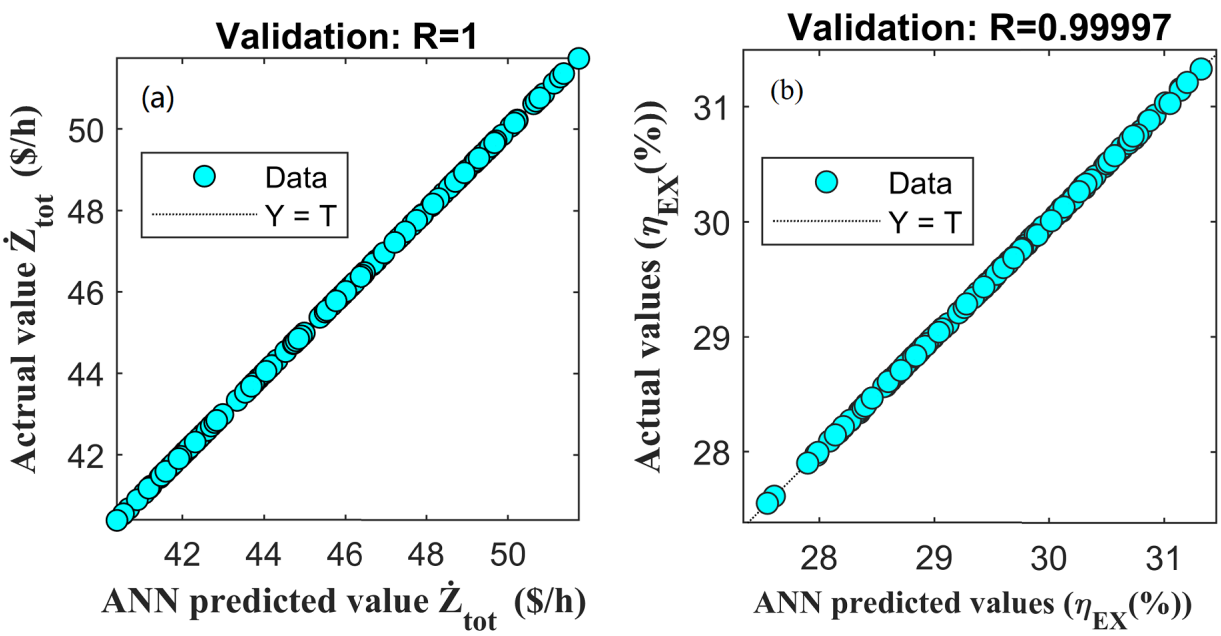

Figure 3. The validation result of the total cost $\dot{Z}_{tot}$ (**a**) and the exergy efficiency η_{EX} (**b**).

4.1. Validation

Recognizing the innovative nature of the proposed system, a rigorous validation of its pivotal components was undertaken to uphold the accuracy of the analytical conclusions. Subsystem validation was executed independently, utilizing published data from Yu [26] and Yang [60]. In Table 5, a comprehensive comparison is presented between the outcomes of the present investigation and the findings reported in these references concerning the ORC cycle, revealing remarkable congruity with the conclusions elucidated in the cited work.

Table 5. Validation detail for the proposed system.

	T_{HT} (°C)	T_{CT} (°C)	P_{EVA} (bar)	T_{Tur}^{inlet} (°C)	η_{ORC} (%)	η_{sys} (%)
Yang et al. [60]	375	71.7	37.12	311.5	22.2	14.9
This work	375	71.7	37.12	311.5	22.2	14.82
Yu et al. [26]	368	57.6	37.12	313.3	24.3	17.4
This work	368	57.6	37.12	313.3	24.3	16.3

4.2. Parametric Analysis

In this endeavor, the primary objective is to identify the design elements that exert the most significant influence on the performance of the system. The impact of T_{15} and T_{10} on the chosen performance goals of the suggested system is depicted in Figure 4. The range of T_{15} is from 70 to 90 °C. Notably, in Figure 4a, it is evident that both η_{EX} and $\dot{Z}_{tot}$ exhibit a decline as T_{15} increases. The variation range of η_{EX} is from 30.44% to 30.07%; meanwhile, the maximum value of $\dot{Z}_{tot}$ is US$39.4/h, and the minimum value of $\dot{Z}_{tot}$ is US$39.09/h. The inlet temperature of the turbine (T_{10}) also has a great influence on the performance of the system. Figure 4b reveals that both η_{EX} and $\dot{Z}_{tot}$ exhibit an increase as T_{10} rises. Notably, at a T_{10} value of 280 °C, both η_{EX} and $\dot{Z}_{tot}$ reach their maximum values of 30.52% and US$39.44/h, respectively. The desired minimum value of $\dot{Z}_{tot}$, however, is attained at T_{10}= 240 °C, where it reaches US$38.11/h. The variables T_{15} and T_{10} are intricately tied to the system's heat absorption amount. Elevated T_{10} values coupled with lower T_{15} values signify enhanced heat transfer, resulting in heightened exergy efficiency. It is important to note that a larger heat transfer area corresponds to increased costs.

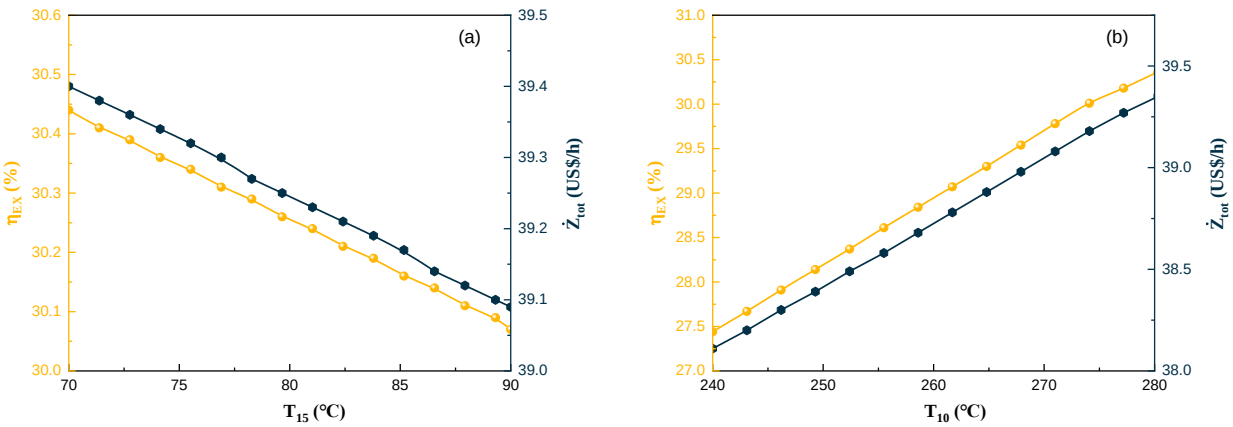

Figure 4. Contribution of output temperature of TEG T_{15} (**a**) and inlet temperature of turbine T_{10} (**b**) with the exergy efficiency and total cost of the system.

The performance of the system is greatly influenced by the total area of the solar collector (A_{tot}) and the temperature of the output WF (T_2). Figure 5 illustrates the relationship between η_{EX} and $\dot{Z}_{tot}$ with respect to A_{tot} and T_2. In Figure 5a, it is evident that η_{EX} increases as A_{tot} increases. The maximum value of η_{EX}, reaching 31.65%, is observed when A_{tot} equals 9000. Simultaneously, $\dot{Z}_{tot}$ also shows an increasing trend, with a minimum

value of US$35.54/h. In Figure 5b, η_{EX} and $\dot{Z}_{tot}$ decrease as T_2, the maximum value of η_{EX} is 30.83% and, furthermore, the minimum value of $\dot{Z}_{tot}$ is US$39.06/h. Based on the above analysis, achieving a higher η_{EX} can be accomplished by increasing A_{tot} and T_{10} while decreasing T_2 and T_{15}. In contrast, lower $\dot{Z}_{tot}$ can be realized by increasing T_2 and T_{15} while decreasing A_{tot} and T_{10}. In order to strike a balance between higher efficiency and lower cost, it becomes apparent that both cannot be achieved simultaneously. Therefore, the modeling process incorporates optimization techniques to find an optimal solution.

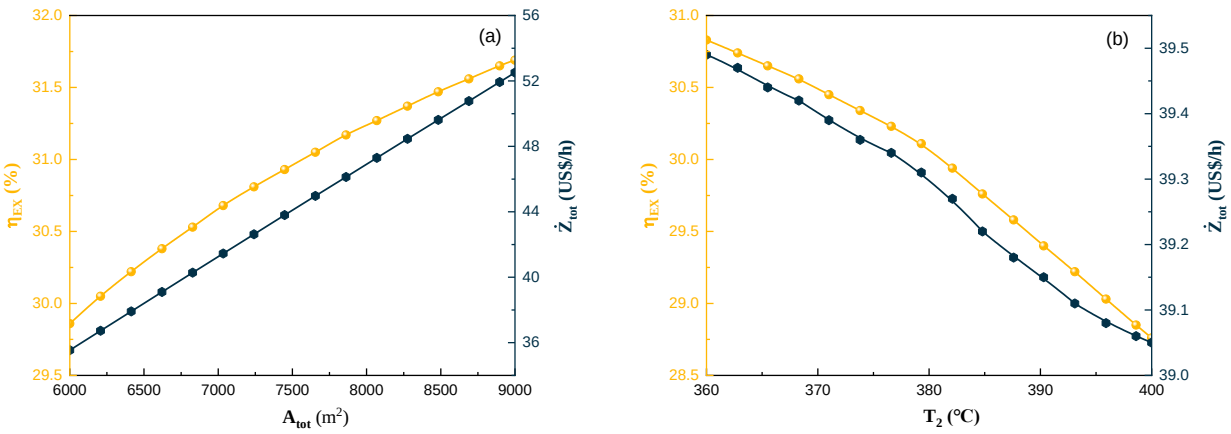

Figure 5. The influence of the area of the solar collector A_{tot} (**a**) and the outlet temperature of solar collector T_2 (**b**) on the exergy efficiency and total cost of the system.

4.3. Multi-Objective Optimization

The performance of the ORC is influenced by a wide range of factors. The performance metrics or expenses typically increase or decrease in tandem with these parameters. For this reason, the best design point should be discovered via multi-objective optimization. Many challenging engineering optimization issues can be realistically modeled using multi-objective optimization. Because minimizing cost and maximizing performance are sometimes at odds with one another in real-world problems, using the single-objective approach to optimize a particular state can produce unexpected outcomes when compared to other objective functions. Two optimization goal functions for the ORC design have been chosen for this work. The primary objective function is to increase the cycle's exergy efficiency, which is computed using η_{EX}, and the second objective function is to minimize the initial hourly cost of the system $\dot{Z}_{tot}$. Based on the parametric analysis, four design variables were chosen to be the input parameter for optimization.

In the present study, the NSGA-II algorithm is employed to obtain the optimal solution. Throughout the process, a population of distinct solutions is iteratively modified. At each stage, individuals are randomly selected from the existing population to act as parents and produce offspring for future generations. The population gradually adapts toward the best solution across subsequent generations. For this study, the population size is 200, and the maximum number of generations is 100. Details of the parameters are shown in Table 6.

Table 6. The control parameters during the optimal process in NSGA-II.

Parameters	Value
Population size	200
Crossover fraction	0.7
Selection process	Tournament
Migration fraction	0.4
Maximum generation	100

The Pareto frontier solution for the proposed system obtained through NSGA-II is shown in Figure 6, which amply illustrates the conflict between two objectives—η_{EX} and $\dot{Z}_{tot}$. The $\dot{Z}_{tot}$ rises whenever a thermodynamic parameter boosts the η_{EX}. The highest η_{EX} is present at design point A because this is where the $\dot{Z}_{tot}$ is highest. On the other side, design point B has the lowest $\dot{Z}_{tot}$ and the lowest η_{EX}. When energy efficiency is a single goal function, design point A represents the ideal circumstance, whereas design point B represents the ideal situation when the hourly cost is a single objective function.

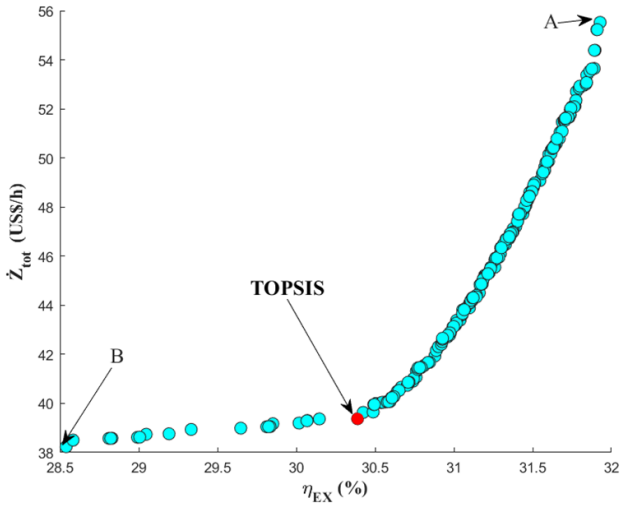

Figure 6. The Pareto frontier for hourly cost and exergy efficiency using NSGA-II.

All the solutions are the best choice for the proposed system, and the TOPSIS decision-maker is used to choose the ideal point. Optimization result details are shown in Table 7. The ideal point chosen by TOPSIS corresponds to the values of US$39.38/h for $\dot{Z}_{tot}$ and 30.39% for η_{EX}, respectively. Simultaneously, the system exhibits a total output power of 577.9 kJ/kg, a mass flow rate of fresh water of 137.7 m^3/h, and a district heating supply of 1074 kJ/kg.

Table 7. Optimization details for the TOPSIS ideal point.

Parameters	TOPSIS Value	Point A	Point B
T_{15} (°C)	70.92	70.00	84.48
T_2 (°C)	371.89	370.63	379.11
T_{10} (°C)	281.50	282.11	263.06
A_{Tol} (m^2)	6671.55	9535.19	6668.21
η_{EX} (%)	30.39	31.93	28.58
$\dot{Z}_{tot}$ (US$/h)	39.38	55.53	38.50
$\dot{W}_{net}$ (kJ/kg)	577.9	869.5	516
$\dot{m}_{FW}$ (m^3/h)	137.7	183.8	126.8
$\dot{Q}_{DH}$ (kJ/kg)	1074	1606	1090

4.4. Cost Analysis

The cost diagram, presented in Figure 7, provides a visual representation of the cost breakdown, while Table 8 provides detailed information. Notably, the solar collector stands out as the most expensive component, amounting to US$26.77/h, representing approximately 68% of the total cost. Following closely, the turbine incurs the second highest cost at US$6.185/h, accounting for approximately 15.7% of the total cost. The third and fourth most expensive units within the system are the TEG and RO, with costs of US$2.318/h and US$2.256/h, respectively. These costs represent approximately 5.9% and 5.7% of the total system cost, respectively. The ORC system is composed of several integral components,

including an economizer, evaporator, HEX, OFOH, pump, and turbine. Notably, the investment cost of the ORC system amounts to US$8.0377/h, accounting for approximately 20.4% of the overall system cost.

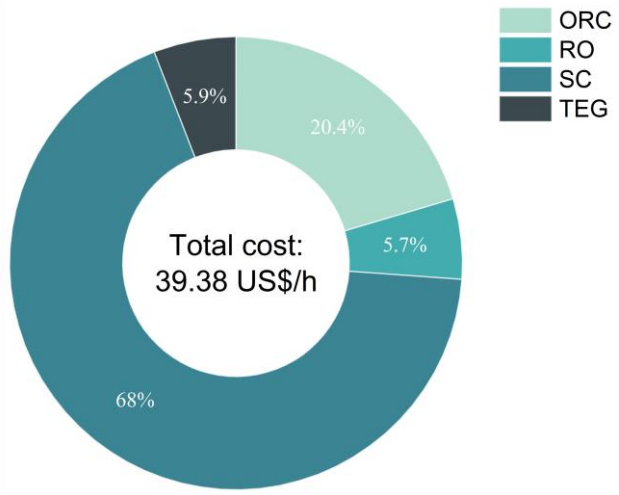

Figure 7. Cost diagram of the system.

Table 8. The hourly cost of each element.

Elements	Hourly Cost (US$/h)	Percentage (%)
Economizer	0.4516	1.1
Evaporator	0.3365	0.9
HEX	0.2275	0.6
OFOH	0.2964	0.8
Pump	0.5407	1.4
Turbine	6.185	15.7
RO	2.256	5.7
TEG	2.318	5.9
Solar collector	26.77	68

The primary cost factor is associated with the solar cycle. Future efforts should prioritize the reduction of solar collector costs and explore hybrid systems, such as a solar–geothermal hybrid system, which could offer a more effective solution. Furthermore, in contrast to prior studies, ANN is employed for optimization in this work. This approach tackles complex calculation challenges and notably diminishes computation time. The ANN plays a crucial role in streamlining the thermodynamic model. Both the HE and TEG have been seamlessly integrated into the system, effectively enhancing the overall efficiency of the ORC.

5. Conclusions

An investigation was conducted to compare the thermodynamic performance and economic parameters of a PTC (Parabolic Trough Collector) powered ORC (Organic Rankine Cycle) using DowthermA and toluene. The study employed thermo-economic multi-objective optimization and decision-making techniques. Four key parameters, namely the outlet temperature of the solar collector (T_2), turbine inlet temperature (T_{10}), TEG outlet temperature (T_{15}), and overall area of the solar collector (A_{tot}), were analyzed to determine their impact on the system's exergy efficiency and hourly cost.

Through the application of TOPSIS decision-making, the Pareto-optimal solutions were identified from the Pareto-optimal frontier. The investigation yielded several notable findings, which can be summarized as follows:

- The exergy efficiency (η_{EX}) and hourly total cost ($\dot{Z}_{tot}$) exhibit a decrease when the temperatures T_2 and T_{15} increase. Conversely, an increase in η_{EX} and $\dot{Z}_{tot}$ is observed with higher temperatures T_{10} and A_{tot}.
- The NSGA-II algorithm is employed for the optimization process, resulting in a Pareto frontier. From this frontier, the range of η_{EX} is found to be between 28.58% and 31.93%, while the range of $\dot{Z}_{tot}$ spans from US$38.5/h to US$55.53/h.
- Utilizing TOPSIS decision-making, the best solution from the Pareto frontier is determined, with η_{EX} and $\dot{Z}_{tot}$ values of 30.39% and US$39.38/h, respectively. Additionally, the system parameters include a mass flow rate of fresh water at 137.7 m^3/h, a total output net power of 577.9 kJ/kg, and a district heating supply of 1074 kJ/kg.
- A detailed breakdown of the cost rates for each component reveals that the solar collector accounts for US$26.77/h, representing approximately 68% of the total hourly cost. The subsequent components in terms of cost are the ORC, TEG, and RO units.

Moreover, it is essential to acknowledge several limitations within this research. Notably, the system optimization was exclusively performed under design conditions, with off-design operations not being considered. To address this, extending the analysis to encompass dynamic simulations would enable the capture of transient behaviors and facilitate the evaluation of system responses across diverse operational scenarios. This expansion will facilitate a deeper and more comprehensive understanding of the intricate dynamics that are inherent to the system.

Author Contributions: Conceptualization, methodology, software, writing—original draft preparation, L.W.; validation, formal analysis, investigation, C.Z.; resources, data curation, writing—review and editing, visualization, supervision, project administration, H.R.R. All authors have read and agreed to the published version of the manuscript.

Funding: This research was funded by the Basic Scientific Research Project of Colleges and Universities of Liaoning Provincial Department of Education (JL202014).

Institutional Review Board Statement: Not applicable.

Informed Consent Statement: Not applicable.

Data Availability Statement: The data supporting this study's findings are available from the corresponding author upon reasonable request.

Acknowledgments: The authors express their gratitude to Seyed Mojtaba Alirahmi for technical support.

Conflicts of Interest: The authors declare that there is no conflict of interest.

References

1. Bozgeyik, A.; Altay, L.; Hepbasli, A. A Parametric Study of a Renewable Energy Based Multigeneration System Using PEM for Hydrogen Production with and without Once-through MSF Desalination. *Int. J. Hydrogen Energy* **2022**, *47*, 31742–31754. [CrossRef]
2. Geng, D.; Cui, J.; Fan, L. Performance Investigation of a Reverse Osmosis Desalination System Powered by Solar Dish-Stirling Engine. *Energy Rep.* **2021**, *7*, 3844–3856. [CrossRef]
3. Ahmed, F.E.; Hashaikeh, R.; Hilal, N. Solar Powered Desalination–Technology, Energy and Future Outlook. *Desalination* **2019**, *453*, 54–76. [CrossRef]
4. Liu, Q.; Xu, G.R.; Das, R. Inorganic Scaling in Reverse Osmosis (RO) Desalination: Mechanisms, Monitoring, and Inhibition Strategies. *Desalination* **2019**, *468*, 114065. [CrossRef]
5. Lotfy, H.R.; Staš, J.; Roubík, H. Renewable Energy Powered Membrane Desalination—Review of Recent Development. *Environ. Sci. Pollut. Res.* **2022**, *29*, 46552–46568. [CrossRef] [PubMed]
6. Gorjian, S.; Ghobadian, B.; Ebadi, H.; Ketabchi, F.; Khanmohammadi, S. *Applications of Solar PV Systems in Desalination Technologies*; Elsevier: Amsterdam, The Netherlands, 2020; ISBN 9780128196106.
7. Olabi, A.G.; Abdelkareem, M.A. Renewable Energy and Climate Change. *Renew. Sustain. Energy Rev.* **2022**, *158*, 112111. [CrossRef]
8. Chitgar, N.; Hemmati, A.; Sadrzadeh, M. A Comparative Performance Analysis, Working Fluid Selection, and Machine Learning Optimization of ORC Systems Driven by Geothermal Energy. *Energy Convers. Manag.* **2023**, *286*, 117072. [CrossRef]
9. Tutak, M.; Brodny, J. Renewable Energy Consumption in Economic Sectors in the EU-27. The Impact on Economics, Environment and Conventional Energy Sources. A 20-Year Perspective. *J. Clean. Prod.* **2022**, *345*, 131076. [CrossRef]

10. Pina, E.A.; Lozano, M.A.; Serra, L.M.; Hernández, A.; Lázaro, A. Design and Thermoeconomic Analysis of a Solar Parabolic Trough–ORC–Biomass Cooling Plant for a Commercial Center. *Sol. Energy* **2021**, *215*, 92–107. [CrossRef]
11. Olia, H.; Torabi, M.; Bahiraei, M.; Ahmadi, M.H.; Goodarzi, M.; Safaei, M.R. Application of Nanofluids in Thermal Performance Enhancement of Parabolic Trough Solar Collector: State-of-the-Art. *Appl. Sci.* **2019**, *9*, 463. [CrossRef]
12. Chavez Panduro, E.A.; Finotti, F.; Largiller, G.; Lervåg, K.Y. A Review of the Use of Nanofluids as Heat-Transfer Fluids in Parabolic-Trough Collectors. *Appl. Therm. Eng.* **2022**, *211*, 118346. [CrossRef]
13. Shafiey Dehaj, M.; Rezaeian, M.; Mousavi, D.; Shamsi, S.; Salarmofrad, M. Efficiency of the Parabolic through Solar Collector Using NiFe2O4/Water Nanofluid and U-Tube. *J. Taiwan Inst. Chem. Eng.* **2021**, *120*, 136–149. [CrossRef]
14. Ehyaei, M.A.; Ahmadi, A.; El Haj Assad, M.; Salameh, T. Optimization of Parabolic through Collector (PTC) with Multi Objective Swarm Optimization (MOPSO) and Energy, Exergy and Economic Analyses. *J. Clean. Prod.* **2019**, *234*, 285–296. [CrossRef]
15. Casati, E.; Galli, A.; Colonna, P. Thermal Energy Storage for Solar-Powered Organic Rankine Cycle Engines. *Sol. Energy* **2013**, *96*, 205–219. [CrossRef]
16. Nondy, J.; Gogoi, T.K. Exergoeconomic Investigation and Multi-Objective Optimization of Different ORC Configurations for Waste Heat Recovery: A Comparative Study. *Energy Convers. Manag.* **2021**, *245*, 114593. [CrossRef]
17. Bahrami, M.; Pourfayaz, F.; Kasaeian, A. Low Global Warming Potential (GWP) Working Fluids (WFs) for Organic Rankine Cycle (ORC) Applications. *Energy Rep.* **2022**, *8*, 2976–2988. [CrossRef]
18. Li, X.; Xu, B.; Tian, H.; Shu, G. Towards a Novel Holistic Design of Organic Rankine Cycle (ORC) Systems Operating under Heat Source Fluctuations and Intermittency. *Renew. Sustain. Energy Rev.* **2021**, *147*, 111207. [CrossRef]
19. Peng, Y.; Lin, X.; Liu, J.; Su, W.; Zhou, N. Machine Learning Prediction of ORC Performance Based on Properties of Working Fluid. *Appl. Therm. Eng.* **2021**, *195*, 117184. [CrossRef]
20. Jamshidian, F.J.; Gorjian, S.; Shafieefar, M. Techno-Economic Assessment of a Hybrid RO-MED Desalination Plant Integrated with a Solar CHP System. *Energy Convers. Manag.* **2022**, *251*, 114985. [CrossRef]
21. Elsaid, K.; Kamil, M.; Sayed, E.T.; Abdelkareem, M.A.; Wilberforce, T.; Olabi, A. Environmental Impact of Desalination Technologies: A Review. *Sci. Total Environ.* **2020**, *748*, 141528. [CrossRef]
22. Lattemann, S.; Höpner, T. Environmental Impact and Impact Assessment of Seawater Desalination. *Desalination* **2008**, *220*, 1–15. [CrossRef]
23. Mito, M.T.; Ma, X.; Albuflasa, H.; Davies, P.A. Reverse Osmosis (RO) Membrane Desalination Driven by Wind and Solar Photovoltaic (PV) Energy: State of the Art and Challenges for Large-Scale Implementation. *Renew. Sustain. Energy Rev.* **2019**, *112*, 669–685. [CrossRef]
24. Jafary, S.; Khalilarya, S.; Shawabkeh, A.; Wae-hayee, M.; Hashemian, M. A Complete Energetic and Exergetic Analysis of a Solar Powered Trigeneration System with Two Novel Organic Rankine Cycle (ORC) Configurations. *J. Clean. Prod.* **2021**, *281*, 124552. [CrossRef]
25. Aliahmadi, M.; Moosavi, A.; Sadrhosseini, H. Multi-Objective Optimization of Regenerative ORC System Integrated with Thermoelectric Generators for Low-Temperature Waste Heat Recovery. *Energy Rep.* **2021**, *7*, 300–313. [CrossRef]
26. Yu, H.; Helland, H.; Yu, X.; Gundersen, T.; Sin, G. Optimal Design and Operation of an Organic Rankine Cycle (ORC) System Driven by Solar Energy with Sensible Thermal Energy Storage. *Energy Convers. Manag.* **2021**, *244*, 114494. [CrossRef]
27. Li, Z.; Huang, R.; Lu, Y.; Roskilly, A.P.; Yu, X. Analysis of a Combined Trilateral Cycle-Organic Rankine Cycle (TLC-ORC) System for Waste Heat Recovery. *Energy Procedia* **2019**, *158*, 1786–1791. [CrossRef]
28. Razmi, A.R.; Alirahmi, S.M.; Nabat, M.H.; Assareh, E.; Shahbakhti, M. A Green Hydrogen Energy Storage Concept Based on Parabolic Trough Collector and Proton Exchange Membrane Electrolyzer/Fuel Cell: Thermodynamic and Exergoeconomic Analyses with Multi-Objective Optimization. *Int. J. Hydrogen Energy* **2022**, *47*, 26468–26489. [CrossRef]
29. Rostami, M.; Manshadi, M.D.; Afshari, E. Energy Production and Storage from a Polygeneration System Based on Parabolic Trough Solar Collector, Proton Exchange Membrane Fuel Cell, Organic Rankine Cycle, and Alkaline Electrolyzer. *J. Energy Storage* **2022**, *47*, 103635. [CrossRef]
30. Alotaibi, S.; Alotaibi, F.; Ibrahim, O.M. Solar-Assisted Steam Power Plant Retrofitted with Regenerative System Using Parabolic Trough Solar Collectors. *Energy Rep.* **2020**, *6*, 124–133. [CrossRef]
31. Richards, B.S.; Capão, D.P.S.; Früh, W.G.; Schäfer, A.I. Renewable Energy Powered Membrane Technology: Impact of Solar Irradiance Fluctuations on Performance of a Brackish Water Reverse Osmosis System. *Sep. Purif. Technol.* **2015**, *156*, 379–390. [CrossRef]
32. Boussouga, Y.A.; Richards, B.S.; Schäfer, A.I. Renewable Energy Powered Membrane Technology: System Resilience under Solar Irradiance Fluctuations during the Treatment of Fluoride-Rich Natural Waters by Different Nanofiltration/Reverse Osmosis Membranes. *J. Memb. Sci.* **2021**, *617*, 118452. [CrossRef]
33. Li, S.; Cai, Y.H.; Schäfer, A.I.; Richards, B.S. Renewable Energy Powered Membrane Technology: A Review of the Reliability of Photovoltaic-Powered Membrane System Components for Brackish Water Desalination. *Appl. Energy* **2019**, *253*, 113524. [CrossRef]
34. Schäfer, A.I.; Richards, B.S. Testing of a Hybrid Membrane System for Groundwater Desalination in an Australian National Park. *Desalination* **2005**, *183*, 55–62. [CrossRef]

35. Shen, J.; Richards, B.S.; Schäfer, A.I. Renewable Energy Powered Membrane Technology: Case Study of St. Dorcas Borehole in Tanzania Demonstrating Fluoride Removal via Nanofiltration/Reverse Osmosis. *Sep. Purif. Technol.* **2016**, *170*, 445–452. [CrossRef]
36. Shekari Namin, A.; Rostamzadeh, H.; Nourani, P. Thermodynamic and Thermoeconomic Analysis of Three Cascade Power Plants Coupled with RO Desalination Unit, Driven by a Salinity-Gradient Solar Pond. *Therm. Sci. Eng. Prog.* **2020**, *18*, 100562. [CrossRef]
37. Dong, R.E.; Zhanguo, S.; Mansir, I.B.; Abed, A.M.; Niu, X. Energy and Exergoeconomic Assessments of a Renewable Hybrid ERC/ORC Integrated with Solar Dryer Unit, PEM Electrolyzer, and RO Desalination Subsystem. *Process Saf. Environ. Prot.* **2023**, *171*, 812–833. [CrossRef]
38. Feng, Y.; Liu, Y.; Wang, X.; He, Z.X.; Hung, T.C.; Wang, Q.; Xi, H. Performance Prediction and Optimization of an Organic Rankine Cycle (ORC) for Waste Heat Recovery Using Back Propagation Neural Network. *Energy Convers. Manag.* **2020**, *226*, 113552. [CrossRef]
39. Zhou, J.; Chu, Y.T.; Ren, J.; Shen, W.; He, C. Integrating Machine Learning and Mathematical Programming for Efficient Optimization of Operating Conditions in Organic Rankine Cycle (ORC) Based Combined Systems. *Energy* **2023**, *281*, 128218. [CrossRef]
40. Chen, W.; Liang, Y.; Luo, X.; Chen, J.; Yang, Z.; Chen, Y. Artificial Neural Network Grey-Box Model for Design and Optimization of 50 MWe-Scale Combined Supercritical CO2 Brayton Cycle-ORC Coal-Fired Power Plant. *Energy Convers. Manag.* **2021**, *249*, 114821. [CrossRef]
41. Verma, S.; Pant, M.; Snasel, V. A Comprehensive Review on NSGA-II for Multi-Objective Combinatorial Optimization Problems. *IEEE Access* **2021**, *9*, 57757–57791. [CrossRef]
42. Ahmadi, P.; Dincer, I.; Rosen, M.A. Multi-Objective Optimization of a Novel Solar-Based Multigeneration Energy System. *Sol. Energy* **2014**, *108*, 576–591. [CrossRef]
43. Oyekale, J.; Petrollese, M.; Cau, G. Multi-Objective Thermo-Economic Optimization of Biomass Retrofit for an Existing Solar Organic Rankine Cycle Power Plant Based on NSGA-II. *Energy Rep.* **2020**, *6*, 136–145. [CrossRef]
44. Xu, C.; Ke, Y.; Li, Y.; Chu, H.; Wu, Y. Data-Driven Configuration Optimization of an off-Grid Wind/PV/Hydrogen System Based on Modified NSGA-II and CRITIC-TOPSIS. *Energy Convers. Manag.* **2020**, *215*, 112892. [CrossRef]
45. Hwang, C.-L.; Yoon, K. *Multiple Attribute Decision Making: Methods and Applications*; Springer: Berlin/Heidelberg, Germany; New York, NY, USA, 1981.
46. Tiwari, D.; Sherwani, A.F.; Muqeem, M.; Goyal, A. Parametric Optimization of Organic Rankine Cycle Using TOPSIS Integrated with Entropy Weight Method. *Energy Sources Part A Recover. Util. Environ. Eff.* **2022**, *44*, 2430–2447. [CrossRef]
47. Alirahmi, S.M.; Ebrahimi-Moghadam, A. Comparative Study, Working Fluid Selection, and Optimal Design of Three Systems for Electricity and Freshwater Based on Solid Oxide Fuel Cell Mover Cycle. *Appl. Energy* **2022**, *323*, 119545. [CrossRef]
48. Xi, Z.; Eshaghi, S.; Sardari, F. Energy, Exergy, and Exergoeconomic Analysis of a Polygeneration System Driven by Solar Energy with a Thermal Energy Storage Tank for Power, Heating, and Freshwater Production. *J. Energy Storage* **2021**, *36*, 102429. [CrossRef]
49. Alirahmi, S.M.; Assareh, E. Energy, Exergy, and Exergoeconomics (3E) Analysis and Multi-Objective Optimization of a Multi-Generation Energy System for Day and Night Time Power Generation-Case Study: Dezful City. *Int. J. Hydrogen Energy* **2020**, *45*, 31555–31573. [CrossRef]
50. Jouhara, H.; Żabnieńska-Góra, A.; Khordehgah, N.; Doraghi, Q.; Ahmad, L.; Norman, L.; Axcell, B.; Wrobel, L.; Dai, S. Thermoelectric Generator (TEG) Technologies and Applications. *Int. J. Thermofluids* **2021**, *9*, 100063. [CrossRef]
51. Mahmoudan, A.; Esmaeilion, F.; Hoseinzadeh, S.; Soltani, M.; Ahmadi, P.; Rosen, M. A Geothermal and Solar-Based Multigeneration System Integrated with a TEG Unit: Development, 3E Analyses, and Multi-Objective Optimization. *Appl. Energy* **2022**, *308*, 118399. [CrossRef]
52. Alirahmi, S.M.; Rostami, M.; Farajollahi, A.H. Multi-Criteria Design Optimization and Thermodynamic Analysis of a Novel Multi-Generation Energy System for Hydrogen, Cooling, Heating, Power, and Freshwater. *Int. J. Hydrogen Energy* **2020**, *45*, 15047–15062. [CrossRef]
53. Abbasi, H.R.; Pourrahmani, H. Multi-Objective Optimization and Exergoeconomic Analysis of a Continuous Solar-Driven System with PCM for Power, Cooling and Freshwater Production. *Energy Convers. Manag.* **2020**, *211*, 112761. [CrossRef]
54. Alirahmi, S.M.; Behzadi, A.; Ahmadi, P.; Sadrizadeh, S. An Innovative Four-Objective Dragonfly-Inspired Optimization Algorithm for an Efficient, Green, and Cost-Effective Waste Heat Recovery from SOFC. *Energy* **2023**, *263*, 125607. [CrossRef]
55. Zahedi, R.; Ahmadi, A.; Dashti, R. Energy, Exergy, Exergoeconomic and Exergoenvironmental Analysis and Optimization of Quadruple Combined Solar, Biogas, SRC and ORC Cycles with Methane System. *Renew. Sustain. Energy Rev.* **2021**, *150*, 111420. [CrossRef]
56. Amid, S.; Aghbashlo, M.; Tabatabaei, M.; Karimi, K.; Nizami, A.S.; Rehan, M.; Hosseinzadeh-Bandbafha, H.; Mojarab Soufiyan, M.; Peng, W.; Lam, S.S. Exergetic, Exergoeconomic, and Exergoenvironmental Aspects of an Industrial-Scale Molasses-Based Ethanol Production Plant. *Energy Convers. Manag.* **2021**, *227*, 113637. [CrossRef]
57. Teng, S.; Wang, M.; Xi, H.; Wen, S. Energy, Exergy, Economic (3E) Analysis, Optimization and Comparison of Different ORC Based CHP Systems for Waste Heat Recovery. *Case Stud. Therm. Eng.* **2021**, *28*, 101444. [CrossRef]
58. da Silva Morais, P.H.; Lodi, A.; Aoki, A.C.; Modesto, M. Energy, Exergetic and Economic Analyses of a Combined Solar-Biomass-ORC Cooling Cogeneration Systems for a Brazilian Small Plant. *Renew. Energy* **2020**, *157*, 1131–1147. [CrossRef]

59. Lee, J.M.; Hong, S.H.; Seo, B.M.; Lee, K.H. Application of Artificial Neural Networks for Optimized AHU Discharge Air Temperature Set-Point and Minimized Cooling Energy in VAV System. *Appl. Therm. Eng.* **2019**, *153*, 726–738. [CrossRef]
60. Yang, J.; Li, J.; Yang, Z.; Duan, Y. Thermodynamic Analysis and Optimization of a Solar Organic Rankine Cycle Operating with Stable Output. *Energy Convers. Manag.* **2019**, *187*, 459–471. [CrossRef]